Chapter 3

Parametric Resonance

Emergence of long-term temporal order in a system of parametrically-pumped electron oscillators may be regarded as a dissipative structure [65] (whose coherent behaviors can only be maintained with sufficient flow of energy). Familiar dissipative structures include the Rayleigh-Benard instability in convection cells and the laser instability [17]. For example, it is well-known that the laser behaves like an ordinary lamp if the pump is weak, and hence the output is low and incoherent. But when the pump power exceeds a threshold, the power and coherence time of the laser output increase by many orders of magnitude.

Parametric excitation, except in an experiment with one electron [92], has been used to increase the disordered internal motions of stored ions or electrons [18,93]. In the new regime which is studied here, parametrically-pumped electron oscillators respond stochastically at a low level until the electrons are cooled via radiation into the microwave cavity whereupon strong coherent oscillations are observed. Cooling by the LCr circuit does not suffice. However, electron-electron collisions transfer some internal energy to the cyclotron motions of the electrons. This energy is removed by coupling the cyclotron oscillators to a resonant mode of the cold, cylindrical cavity (Chapter 4). Throughout this chapter, radiative cooling of the electron oscillators has been maximized by tuning the cyclotron frequency into resonance with the eigenfrequency of a cavity mode, such as TE_{115}. Later chapters will discuss what happens when the electrons are not resonantly

cooled by the microwave cavity.

3.1 Transition to Coherent Oscillations

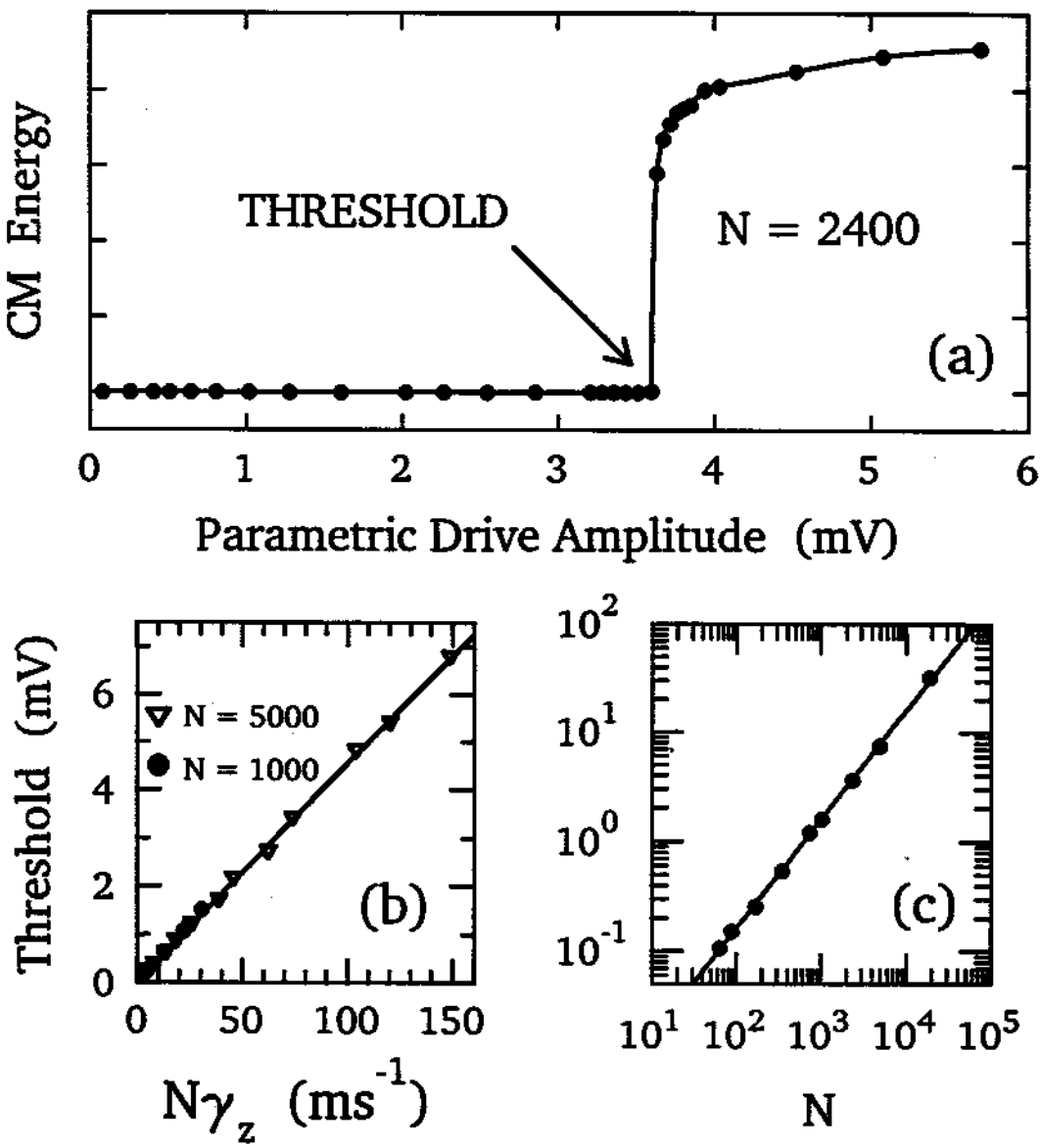

Figure 3.1: Observation of abrupt transition from weak, disordered motions to large, coherent CM oscillation at a pump strength threshold (a). Measured threshold varies linearly with damping rate (b) and with the number of electrons (c).

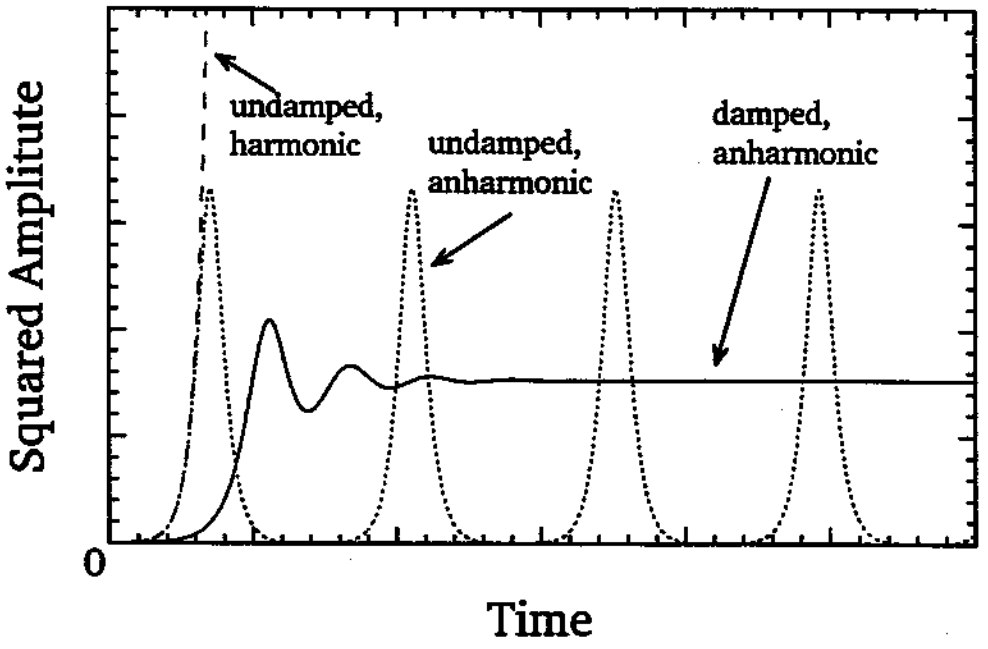

Figure 3.2: Parametric resonance with characteristic exponential growth of harmonic oscillation (dashed line). Periodic variation results as anharmonicity arrests growth (dotted line) but damping causes relaxation to steady state (solid line).

Cooled electrons switch abruptly from independent, stochastic motions to a highly synchronized motion with a greatly increased center-of-mass (CM) amplitude (Fig. 3.1a) as the strength of the parametric pump at $\omega_d = 2\omega_z$ is increased by less than 0.5 dB across the threshold $h = h_T$. The amplitude of the CM motion increases by orders of magnitude and this motion is phase coherent with the subharmonic of the drive at $\omega_d/2$ (coherence time $> 1000s$ for $N > 2000$ electrons). Fig. 3.1b shows that $h_T \propto N\gamma_z$ by detuning ω_z from resonance with the LCR circuit to change γ_z (as illustrated earlier in Fig. 2.16) and by varying the electron number between $N = 60$ and $N = 18,000$ (Fig. 3.1c). Logarithmic scales are used in Fig. 3.1c to show the linear dependence over many orders of magnitude.

These observations suggest that the parametric drive is exciting an insta-

bility in the collective motion of the N electron oscillators. The full equations of motions are described in Sec. 3.4. To examine some features of the motions, we use a dimensionless CM coordinate $Z = \sum z_i/(Nd)$ where z_i/d is the axial position of the ith electron scaled by a suitable trap dimension. In the limit of vanishing internal energy, the collective motions approach those of a rigid model. A rigid axial motion of N electrons near the trap center has the same differential equation as that for a single particle on axis except with N times larger damping,

$$\begin{aligned} \ddot{Z} + (N\gamma_z)\dot{Z} &+ \tilde{\omega}_z^2[\,1 + h\cos(\omega_d t)\,]Z \\ &+ \frac{2C_4}{1+C_2}\omega_z^2 Z^3 + \frac{3C_6}{1+C_2}\omega_z^2 Z^5 = 0, \end{aligned} \tag{3.1}$$

where h is the pump strength and ω_d is the pump frequency. The nonlinear (anharmonic) terms, with strengths C_4 and C_6, arise from unavoidable or deliberate distortions of the pure electrostatic quadrupole potential [10]. Hence, confined in a pure electrostatic quadrupole, undamped rigid motion would satisfy Mathieu's equation (which is regained from Eq. (3.1) by setting $\gamma_z = C_4 = C_6 = 0$). Mathieu's equation should be a good approximation for small oscillations near the center of actual traps where the restoring force is essentially linear.

It is well-known that the bound solution $Z = 0$ to Mathieu's equation is unstable in some regions of the space (h,ω_d) formed from the pump strength and frequency [1,63]. For small pump strength, $h << 1$, the regions of instability are located near

$$\omega_d = \frac{2\tilde{\omega}_z}{n}. \tag{3.2}$$

We focus only on the $n = 1$ region since higher order instability regions are very narrow and much harder to excite [59]. For pump frequency sufficiently close to $2\omega_z$, any small oscillation grows exponentially without bound (dashed line in Fig. 3.2). In actual Penning traps, however, the residual anharmonicities shift the resonant frequency as the amplitude increases, arresting the rapid growth and causing periodic variation in the amplitude (dotted line in Fig.3.2). With damping

taken into account, the $n = 1$ region of the Mathieu instability is given by

$$-\frac{1}{2}\omega_z\sqrt{h^2 - h_T^2} < \omega_d - 2\tilde{\omega}_z < \frac{1}{2}\omega_z\sqrt{h^2 - h_T^2}\,, \tag{3.3}$$

which has a hyperbolic boundary (Fig. 3.3). This region is smaller for increased damping since the pump must compete with energy dissipation (dashed hyperbola in Fig. 3.3). Inside the hyperbolic region, any small symmetry-breaking fluctuation in the CM location ($Z \neq 0$) increases exponentially but with reduced exponent as the parametric drive overcomes the resistive damping. With the rapid growth arrested by anharmonicities, the damped oscillator relaxes to a steady-state amplitude (Fig.3.2, solid line). Nontrivial steady-state solutions to Eq. (3.1), therefore,

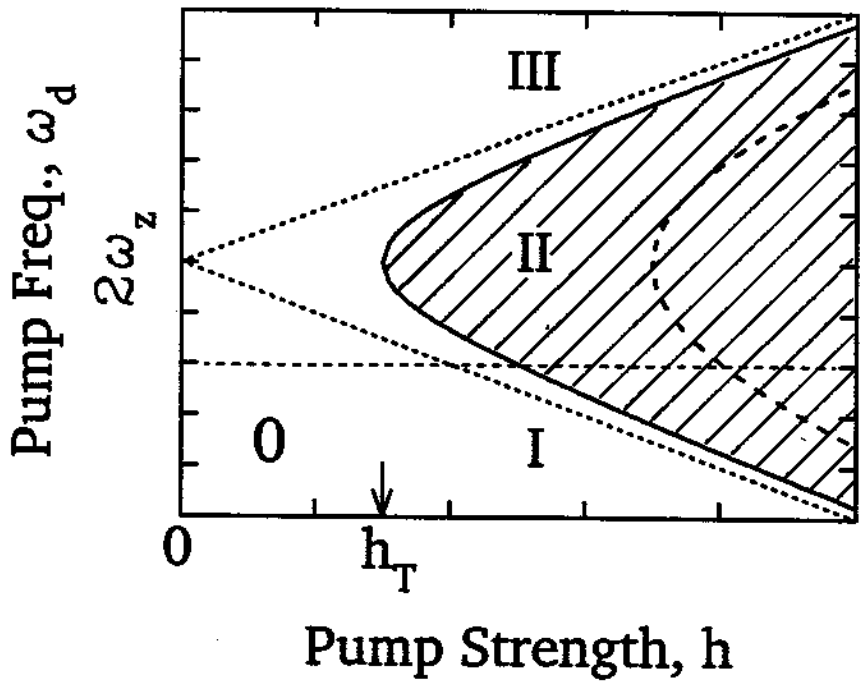

Figure 3.3: Region of $n = 1$ Mathieu instability (shaded) . For $h \ll 1$, a hyperbola divides the neighborhood (h, ω_d) into regions having different sets of stable steady states. For negative C_4 or C_6, region I has 3 stable states; region II, 2 phase bistable exited states; regions III and O, 1 quiescent state.

are limit cycle oscillations [64,59] and

$$h_T \equiv 2N\gamma_z/\omega_z \tag{3.4}$$

is the drive strength h at which there is an abrupt threshold. The observed threshold in Fig. 3.1 corresponds to this vertex of the hyperbolic boundary of the Mathieu instability, which shifts outward with increasing $N\gamma_z$. The measured proportionality constant agrees with Eq. (3.4) within 40% uncertainty.

For an isolated electron ($N = 1$), Eq. (3.1) is an exact description of the unavoidable rigid motion which has been observed [92]. The generalization of Eq. (3.1) which describes the general, nonrigid motion of N electrons has anharmonic terms which depend upon the axial and radial coordinates of the individual electrons (z_i and ρ_i), rather than upon Z alone. For example (see Sec. 3.4), Z^3 becomes $\sum_i (z_i^3 - 3z_i\rho_i^2/2)/N$. Rigid motion of many electrons is typically prevented by the large, stochastically changing coordinates (z_i, ρ_i) of the individual electrons.

Below threshold (i.e. $h < h_T$), $Z = 0$ is the only steady-state solution to Eq.(3.1), and hence is absolutely stable. For the electron cloud, only internal motions (relative to the CM) can therefore be excited by the parametric driving force. Such excitations are occurring, perhaps because the resonant frequencies of internal motions are broadly distributed by the Coulomb repulsion of the electrons, or perhaps because resonant modes of the electron cloud are excited [23], but the exact mechanism is still not understood. Energy coupled into the CM motion by the anharmonic nonlinearities is observed in the form of incoherent transients since such fluctuations (Chapter 5) are damped by the LCR circuit at a rate of order $N\gamma_z$. The coherence time for the detected CM motion is less than 1 ms. This regime is well described by a "bolometric model" which treats the electron cloud as a gas which comes into thermal equilibrium via collisions between electrons [18,93]. However, no synchronized, coherent motion is anticipated or can be accounted for in this model.

Region in (h, ω_d) Space	Stable States	Multiplicity
Region O $(h < h_T)$	1 Quiescent	1
Region I $(h > h_T)$	1 Quiescent + 2 Excited (phase-bistable)	3
Region II $(h > h_T)$	2 Excited (phase-bistable)	2
Region III $(h > h_T)$	1 Quiescent	1

Table 3.1: Multiplicity of stable steady states near $n = 1$ threshold of Mathieu instability. Negative C_4 or C_6 is assumed. For positive C_4 or C_6, regions I and III are interchanged.

3.2 Hysteresis and Lineshapes

In the new regime with $h > h_T$, history-dependent behavior is observed, indicating that the system has more than one stable, collective state above threshold. A hyperbola, Eq.(3.3), divides the parameter space of the pump into 3 distinct regions in the neighborhood of the $n = 1$ instability, according to the multiplicity of stable states which exist above threshold. For simplicity, we discuss the case for $C_4 \leq 0$ and $C_6 \leq 0$ but not both equal zero (Table 3.1 and Fig. 3.3). Below threshold (region O), only the quiescent state ($Z = 0$) is stable. Region I (below the lower branch of the hyperbola in Fig. 3.3)has two degenerate excited states which differ only in phase by 180°, in addition to the quiescent state. Region II (inside the hyperbola in Fig. 3.3) has only the two phase-bistable states because the quiescent state is a saddle-point. As in region O, the quiescent state is the only stable state in Region III (above the upper branch of the the hyperbola in Fig. 3.3). For $C_4 > 0$ or $C_6 > 0$, regions I and III are interchanged.

The "lineshape" of parametric resonance (frequency dependence of the CM energy) varies with anharmonicity and the order in which the pump frequency is swept through these three regions above threshold. Expected lineshapes for the rigid model are shown in Fig. 3.4. Increasing the pump frequency in the order

(I $\longrightarrow$ II $\longrightarrow$ III), the CM energy jumps to a large value as the initial quiescent state becomes unstable in region II. On the other hand, if the pump frequency is decreasing in the order (III $\longrightarrow$ II $\longrightarrow$ I), the system remains in an excited state even though the pump frequency is in Region I. Fluctuations would cause the excited state to collapse to the quiescent state eventually. Different characteristic dependencies of the steady-state amplitude upon the pump frequency is obtained by tuning the trap potentials to make either the C_4 or the C_6 term dominant. For a very anharmonic trap (when C_4 term dominates), the CM energy in the excited

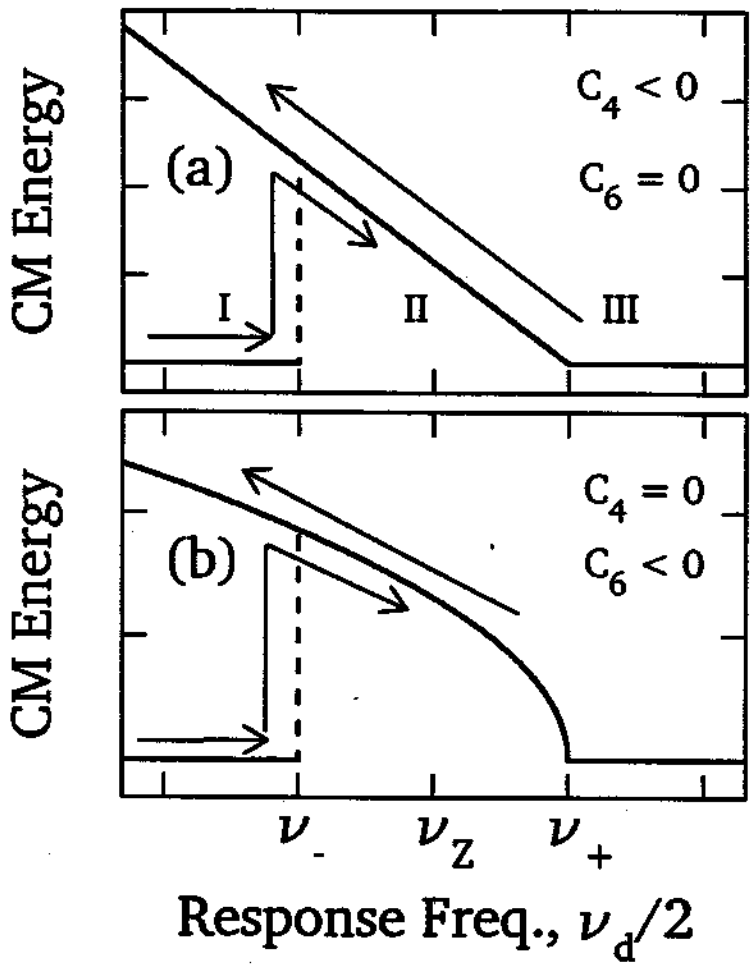

Figure 3.4: Calculated rigid model lineshapes, showing hysteresis of CM energy versus pump frequency ν_d . CM energy is a linear function of pump frequency ν_d for $C_4 < 0$ with $C_6 = 0$ (a), and a parabolic function of ν_d for $C_4 = 0$ with $C_6 < 0$ (b).

state is a linear function of the the pump frequency (Fig. 3.4a). On the other hand, for a well-tuned trap (when $C_4 \approx 0$ and C_6 term dominates), the CM energy for the rigid model is a parabolic function of the pump frequency (Fig. 3.4b). Hysteresis is indeed observed (Fig. 3.5) with resonance "lineshapes" which agrees qualitatively with the rigid model, even though the size of the signal is limited by cavity cooling, an interesting and useful feature which is studied in Chapter 4.

Another type of hysteresis but with fixed pump frequency, is observed when the

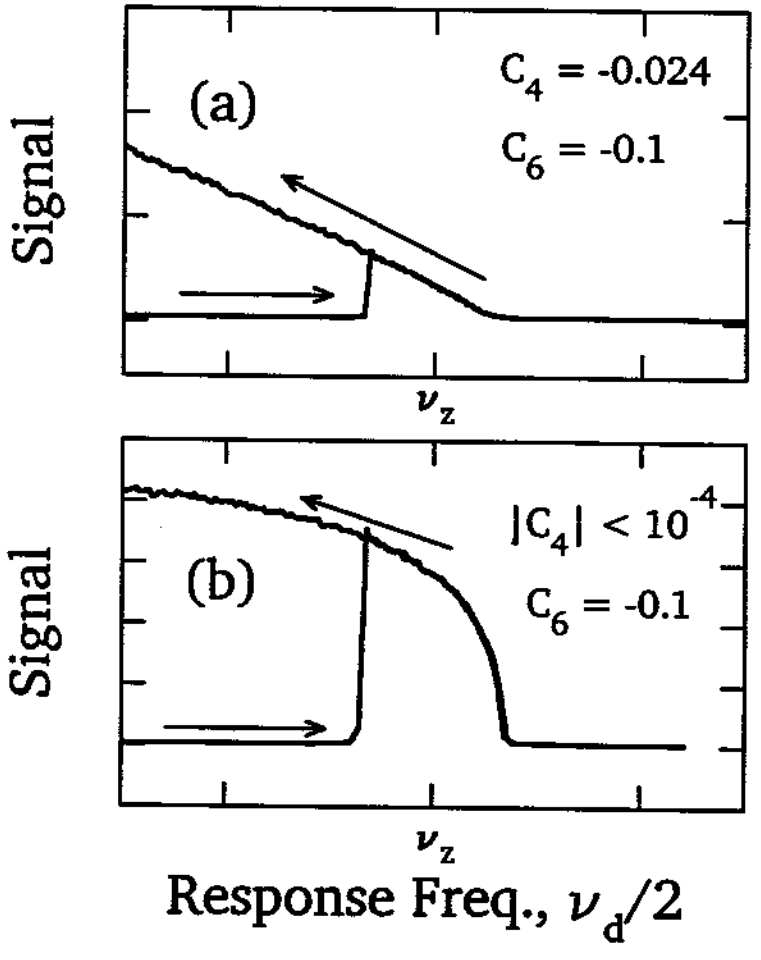

Figure 3.5: Observed resonance lineshapes with hysteresis. Maximum CM energy is limited by cavity-cooling but lineshapes (a) for large C_4 and (b) for negligible C_4 agree qualitatively with rigid model.

pump strength is swept through Regions I and II (e.g., Fig. 3.3, dashed horizontal line). In a rigid model without fluctuations, the system remains in the quiescent state as the pump strength is increased into Region I. It abruptly jumps to an excited state as the pump strength increases across the boundary between Regions I and II. If the pump strength is subsequently decreased into Region I, the excited state remains stable until the pump goes below threshold h_T. Fig.(3.6 a) shows the hysteresis loops observed with synchronized electron oscillators, taken from 4 consecutive sweep cycles (O $\longrightarrow$ I $\longrightarrow$ II $\longrightarrow$ I $\longrightarrow$ O) of the pump strength. Transitions between quiescent and excited states are random due to fluctuations (Chapter 5). The observed distribution (Fig. 3.6 b) of downward transition points (excited to quiescent) shows a narrow spread with small deviations from the threshold h_T in most cases. On the other hand, the observed distribution (Fig. 3.6 b) of upward transition points (quiescent to excited) shows a broader spread with larger deviations from h_U, the boundary point between regions I and II. This seems to suggest that the quiescent state is less stable against fluctuations than the excited states.

The boundary in (h,ω_d) space wherein $Z = 0$ becomes unstable is observed by obtaining a family of resonances at fixed pump strengths above threshold (Fig. 3.7a). The electron oscillators start in the quiescent state in region I. As the pump frequency is increased, the signal jumps abruptly to a large value as $Z = 0$ becomes unstable upon crossing into region II, defining a lower corner frequency $\nu_-(h)$ in Fig. 3.7a. As the pump frequency is increased further, the large signal falls abruptly upon crossing into region III, defining an upper corner frequency $\nu_+(h)$ in Fig. 3.7a. This is repeated for a sequence of fixed pump strengths (illustrated in Fig. 3.7b). The observed range of parametric resonance $[\nu_-(h), \nu_+(h)]$ increases with pump strength h. In agreement with Eq.(3.3) for a rigid model, measured corner frequencies (Fig. 3.7c) lie on a hyperbola when plotted versus pump strength h, with a vertex corresponding to a threshold h_T.

3.3 A Rigid Model

A rigid model neglects many interesting features in order to provide a simple picture. Many important observations which are presented in subsequent chapters can not be described in a rigid model. Nevertheless, it is a useful approximation for some features of the observed coherent motions. Main features of a rigid model have been presented above for comparison with the observed coherent behavior in parametrically-pumped electron oscillators. An exact analysis is difficult but

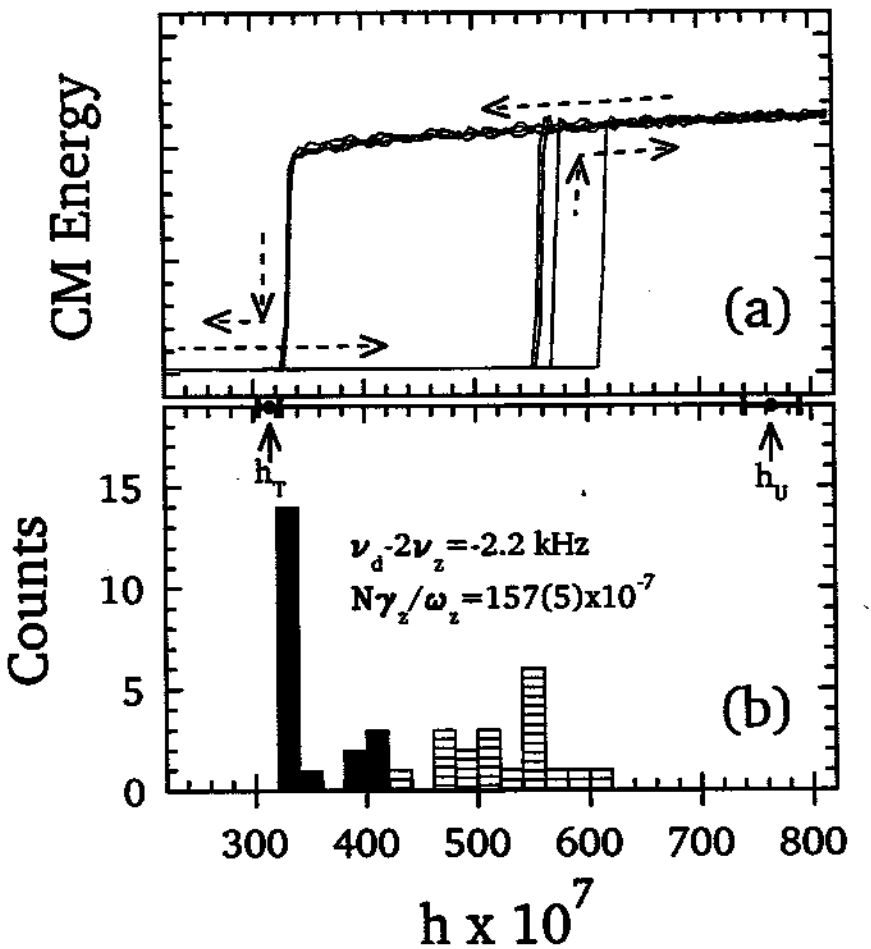

Figure 3.6: (a) Observed hysteresis loops of CM energy versus pump strength in 4 consecutive cycles [O $\longrightarrow$ I $\longrightarrow$ II $\longrightarrow$ I $\longrightarrow$ O]. (b) Histograms of transition points showing that the quiescent state is less stable against fluctuations.

fortunately good approximations are available when the system is weakly damped. This allows the steady state properties to be studied analytically and transient responses to be simulated efficiently. The approximate equations of motion are

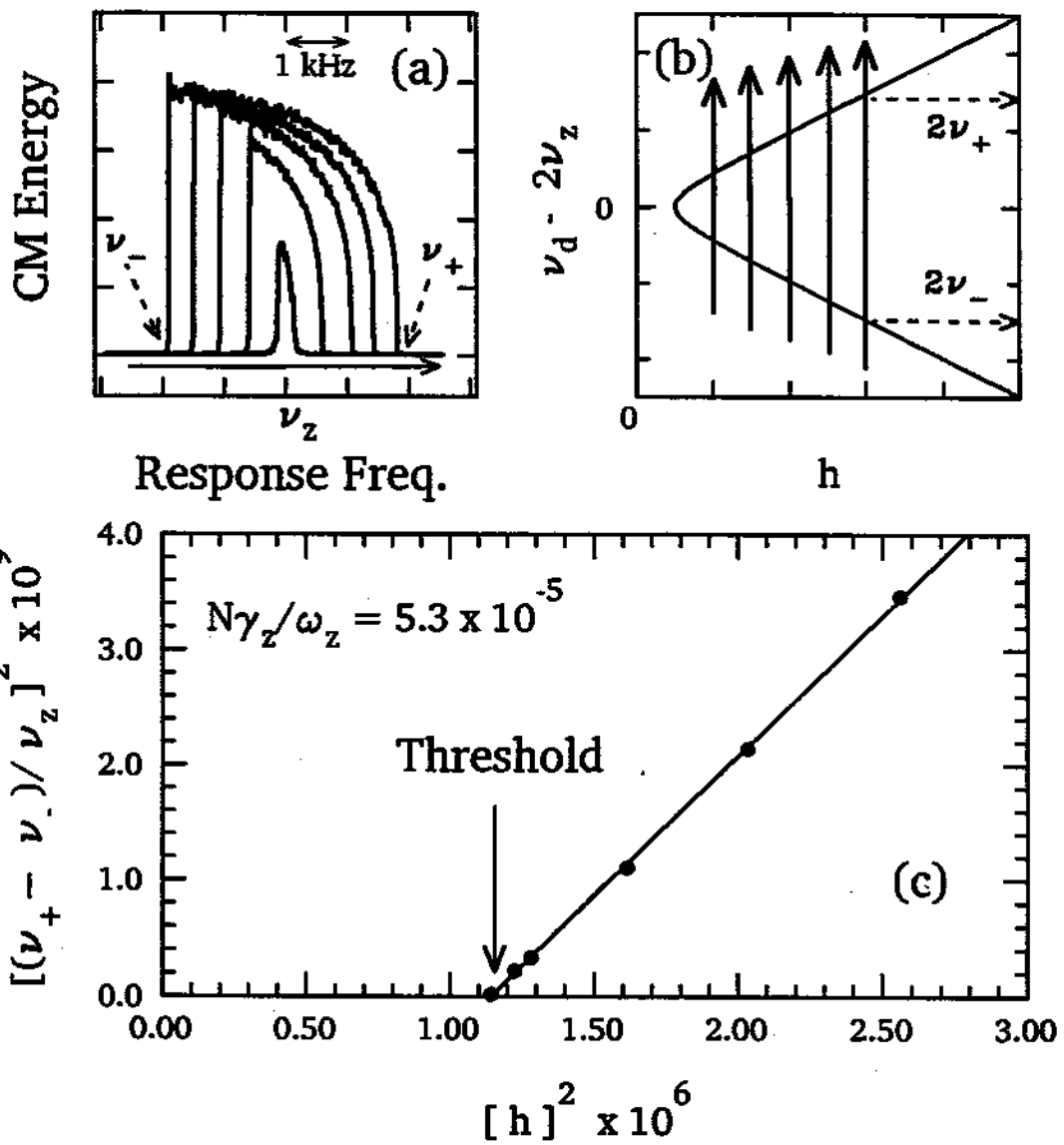

Figure 3.7: Observed frequency range of instability (a) increases with h . Increasing ω_d at fixed h values as illustrated in (b) generates a family of parametric resonances (a). Measured corner frequencies $\nu_+(h)$ and $\nu_-(h)$ fit well to a hyperbola (c) when plotted versus h.

presented in this section with a generalized treatment of the trap anharmonicity and a possible interesting application to one electron (Sec. 3.3.4). The equation of motion Eq. 3.1 is rewritten as

$$0 = \left[\frac{d^2}{dt^2} + N\gamma_z\frac{d}{dt} + (\tilde{\omega}_z)^2(1 + h\cos(2\Omega t))\right] Z(t) + (\omega_z)^2 G(Z) \ , \qquad (3.5)$$

where h is the strength of the parametric drive and 2Ω ($\equiv \omega_d$) is the drive frequency. As before, the coordinate Z is made dimensionless by scaling to the trap size d. To include all orders of deviations (deliberate and unavoidable) from a pure electrostatic quadrupole, the anharmonicity function $G(Z)$ is written as an infinite power series

$$G(Z) = \sigma_4 Z^3 + \sigma_6 Z^5 + \sigma_8 Z^7 + ..., \qquad (3.6)$$

with dimensionless coefficients σ_n which are related to the expansion coefficients C_n of the trapping potential by

$$\sigma_n = \frac{n}{2}\frac{C_n}{1 + C_2}. \qquad (3.7)$$

In compensated Penning traps, C_4 can be made negligibly small using potentials on a set of compensation electrodes (as already discussed). Hence, the two leading terms in the series are used in Eq. (3.1). Since the electron oscillators are weakly damped ($N\gamma_z \ll \omega_z$), a method of multiple time scale [64] may be employed to study Eq.(3.5) in the parameter range of experimental interest. To lowest order in the small parameter $h \ll 1$, we seek solutions at half the frequency of the parametric pump

$$Z(t) = A(t)\ cos[\Omega t + \Psi(t)] + O(h) \ . \qquad (3.8)$$

In this approximation, the slowly varying amplitude $A(t)$ and phase $\Psi(t)$ satisfy a set of coupled first order differential equations

$$\frac{d}{dt}A = -\frac{1}{2}N\gamma_z\left[1 - \frac{h}{h_T}\sin(2\Psi)\right]A, \qquad (3.9)$$

$$\frac{d}{dt}\Psi = (\tilde{\omega}_z - \Omega) + \frac{1}{4}\tilde{\omega}_z h\cos(2\Psi) + J(\{\sigma_i\}, A), \qquad (3.10)$$

derived using a method of multiple time scale [64]. The trap anharmonicity enters these approximate equations of motion through the function

$$J(\{\sigma_i\}, A) = \frac{\omega_z^2}{A\tilde{\omega}_z} \int_0^{2\pi} \frac{d\phi}{2\pi} \cos\phi \; G(A\cos\phi) \quad . \tag{3.11}$$

For example, if $G(Z) = \sigma_4 Z^3$ then

$$J(\sigma_4, A) = \frac{3}{8}\sigma_4 \frac{\omega_z^2}{\tilde{\omega}_z \Omega} A^2. \tag{3.12}$$

We shall use this specific case to illustrate some of the calculations. For example, calculation of growth and relaxation to steady state as shown in Fig. 3.2 is faster using the approximate equations of motion, with results which agree with a direct numerical integration of the exact equation to better than 0.3%.

3.3.1 Steady State Amplitudes

The amplitude of oscillation $A(t)$ will decay for $h < h_T$ because $A^{-1}\dot{A}$ is negative definite, from Eq.(3.9). Hence, below the threshold

$$h_T = 2N\frac{\gamma_z}{\tilde{\omega}_z} \quad , \tag{3.13}$$

the only steady state solution ($\dot{A} = \dot{\Psi} = 0$) is

$$Z(t) = 0. \tag{3.14}$$

For a drive strength above h_T, there are two additional equilibrium amplitudes

$$(A_\pm)^2 \;=\; \frac{4}{3}\frac{1}{\sigma_4}\left[\frac{2(\Omega - \tilde{\omega}_z)}{\tilde{\omega}_z} \pm \frac{1}{2}\sqrt{h^2 - h_T^2}\right]. \tag{3.15}$$

It can be shown that only one choice of the sign gives stable steady-state solutions. Assuming $\sigma_4 < 0$ the negative sign gives stable solutions (Fig. 3.4a). For a well-tuned trap, higher order anharmonicity must be considered. If $G(Z) = \sigma_6 Z^5$ (to approximate a well-tuned trap) then the non-trivial steady states have amplitude given by

$$(A_\pm)^4 \;=\; \frac{8}{5}\frac{1}{\sigma_6}\left[\frac{2(\Omega - \tilde{\omega}_z)}{\tilde{\omega}_z} \pm \frac{1}{2}\sqrt{h^2 - h_T^2}\right], \tag{3.16}$$

with the same sign selection rule (Fig. 3.4b).

3.3.2 Phase Bistability

Resonantly-excited solutions are degenerate because the steady-state phase is determined by the pump only up to $\pm\pi$. This is reflected by the invariance of Eq.(3.9) and Eq.(3.10) under the transformation

$$\Psi \longrightarrow \Psi \pm \pi. \tag{3.17}$$

On the other hand, the phase of steady-state solutions Ψ is given by the condition ($\dot{A} = 0$)

$$\sin(2\Psi_s) \;=\; h_T/h. \tag{3.18}$$

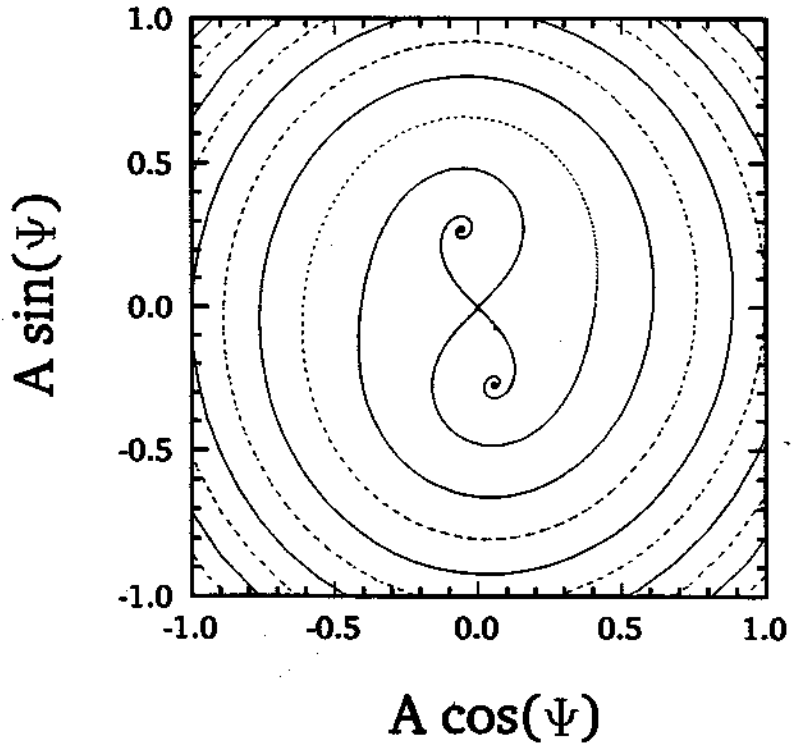

Figure 3.8: Basins of attraction for the two phase states. Quiescent state at the center is a saddle-point.

This is graphically illustrated in Fig. 3.8 which shows the basins of attraction of the two phase states. The saddle-point at the origin is the quiescent state. Phase bistability is manifested by parametrically pumped electron oscillators in interesting ways involving fluctuation phenomena (Chapter 5).

3.3.3 Instability of $Z = 0$ State

As already shown, the quiescent state $Z(t) = 0$ is unstable for some range of system parameters. Without anharmonicity $G(Z)$, the electrons would be ejected from the trap. In actual traps, residual anharmonicity keeps the electrons confined but is not important at the onset of instability which involves only small oscillations. The importance of the tuned circuit is discussed here in some detail. In the absence of the tuned circuit, the rapid exponential growth ($\sim e^{Kt}$) at the onset of the instability is characterized by an exponent given by[59]

$$K = \frac{1}{2}\sqrt{\left(\frac{1}{2}h\omega_z\right)^2 - 4\left(\Omega - \omega_z\right)^2} \tag{3.19}$$

provided that the pump frequency 2Ω is sufficiently near to $2\tilde{\omega}_z$

$$-\frac{1}{2}h\tilde{\omega}_z < 2\Omega - 2\tilde{\omega}_z < \frac{1}{2}h\tilde{\omega}_z \tag{3.20}$$

(region between two dotted lines which intersect at $h = 0$ in Fig. 3.3). However, when the tuned circuit is used for detection, the resonance frequency

$$\omega_z^2 = \frac{qV_o}{md^2}(1 + C_2) \tag{3.21}$$

given in terms of the trapping potential, is shifted slightly ($\omega_z \longrightarrow \tilde{\omega}_z$) because the axial CM motion of the electron oscillators is coupled to a tuned (LCr) circuit. As mentioned earlier, this coupling also damps the CM energy at the rate $N\gamma_z$. If the coupling is not too strong, γ_z and $\tilde{\omega}_z$ are well approximated by simple analytic functions of the detuning between the tuned circuit and electron resonance frequencies, as given in Eq. (2.46) and Eq. (2.47), respectively. Frequency shifts are undesirable in high precision experiments (as discussed in Sec. 4.4). Fortunately, they present a minor inconvenience to our studies because the shifted frequency

and damping rate are determined from a forced resonance of the CM motion as already illustrated in Fig. 2.12. The frequency and strength of the parametric drive are then set using these measured values. In fact, control of the damping rate, according to

$$\gamma_z = \frac{\gamma_{zo}}{1+\delta^2}, \tag{3.22}$$

by changing the detuning δ has been very useful in demonstrating Mathieu instability. Damping stabilizes the quiescent state somewhat as amplification of fluctuations competes with energy dissipation in the tuned circuit, reducing growth in amplitude to $e^{(K-N\gamma_z/2)t}$ (slower initial growth is shown in solid line in Fig. 3.2). The region of parametric resonance ($K - N\gamma_z/2 > 0$) is therefore narrower with a hyperbolic boundary given by Eq. (3.3). As already mentioned, variation of damping rate γ_z using the tuned circuit shows that observed threshold corresponds to the vertex of a hyperbolic boundary.

3.3.4 Hysteresis

When system parameters are changing gradually, hysteresis can occur in nonlinear systems which have multiple stable states with instability under some conditions. The stability of steady states in various ranges of pump strength and frequency (labeled in Fig. 3.3 as O, I, II and III) is summarized in Table 3.1 (for negative σ_k). A sharp transition from one steady state to another occurs when the system parameters are swept slowly into a region wherein the former state becomes unstable. After the transition, if the system is restored to its original conditions by sweeping the parameters through the same path in reverse, the system may remain in the new state or make a transition to the former state under very different conditions. For parametrically-pumped electron oscillators, hysteresis is observed when sweeping the pump frequency with pump strength fixed above threshold (Fig. 3.5) or when sweeping the pump strength with pump frequency fixed below $2\omega_z$ (Fig. 3.6).

Hysteresis can also occur when the pump frequency and strength are fixed

but the oscillator resonance frequency is changing. We illustrate with a possible application for detecting the excitation of a relativistic, mono-electron cyclotron oscillator [31]. The axial resonance frequency

$$\omega_z^2 = \frac{eV_o}{md^2}(1 + C_2) \tag{3.23}$$

is shifted down by an observable amount [31] when the cyclotron oscillator is excited with a microwave drive. This is due to relativistic effects which effectively increase the mass of the electron according to

$$m = \frac{m_o}{\sqrt{1 - (v/c)^2}} \tag{3.24}$$

where m_o is the "rest mass," and v is the velocity of the cyclotron oscillator. Some experiments require knowing if the energy in the cyclotron motion has exceeded a given level within/after a certain period. To detect the corresponding frequency shift $\delta\omega_z$, a parametrically-driven electron is prepared initially in the quiescent state in region I (see Fig. 3.4 and Table 3.1) with the pump frequency fixed at $2\omega_- - 2\delta\omega_z$. As the microwave drive increases the energy in the cyclotron oscillation, region II (wherein $Z = 0$ is unstable) in Fig. 3.4 shifts down toward the drive frequency. When the driven cyclotron oscillator reaches the desired energy level, the quiescent state becomes unstable and the ensuing parametric resonance generates a signal. The signal would persist even if the cyclotron oscillation is subsequently allowed to decay (shifting region II up again). Amplifiers can be turned off to minimize thermal fluctuations during crucial stages of the experiments, and no resonant response to the parametric drive is incurred until the desired level of cyclotron excitation is reached. Briefly, one parametrically-pumped electron oscillator effectively has 1 bit of memory which can be used for detection "in the dark."

3.4 Full Equations of Motion

The rigid model is an accurate description of one electron oscillating along the symmetry axis of the trap. We have demonstrated here that it also provides a

good approximation for many observed features of the coherent CM motions when parametrically-pumped electron oscillators are radiatively cooled by a cold cavity. This rigid model is an oversimplification, however, because it neglects internal and transverse motions entirely, which have important, observable consequences (discussed in following chapters). Without transverse motions, radiative cooling of the internal motions would not be possible. Further, even at 4K (undriven) the thermal motions are more energetic than the average inter-particle Coulomb potential and thus the electrons do not form rigid structures [61]. To understand other interesting observed phenomena which are decidedly non-rigid, a more detailed treatment is required.

Although a thorough analysis of coupled, parametrically-pumped electron oscillators is not yet available, this system is so well-characterized that the full equations of motions of N electrons coupled to 1 cavity mode can be written down. The wide range of experimental control over system parameters allows some simplifications to be made. The k^{th} electron has 3 degrees of freedom $\mathbf{r}_k = (x_k, y_k, z_k)$, which are made dimensionless by scaling to the size of the trap, d. The coupled oscillations parallel to the symmetry axis of the trap (or to the magnetic field) satisfy

$$\begin{aligned} \ddot{z}_k + \quad \gamma_z \textstyle\sum_{i=1}^{N} \quad \dot{z}_i \; + \; \omega_z^2 \, z_k \; + \; \tilde{C}_4 \, \omega_z^2 \, (2z_k^2 - 3\rho_k^2) \, z_k \\ + \quad \tilde{C}_6 \, \omega_z^2 \, (3z_k^4 - 15 z_k^2 \rho_k^4 + \frac{45}{8} \rho_k^4) \, z_k \\ = \; \omega_{ce}^2 \sum_{i \neq k}^{N} \frac{(z_k - z_i)}{|\mathbf{r}_{ik}|^3} \; . \end{aligned} \tag{3.25}$$

Terms with coefficients $\tilde{C}_4$ and $\tilde{C}_6$ are due to deviations from an electric quadrupole potential. To be precise,

$$\tilde{C}_k = \frac{C_k}{1 + C_2} \approx C_k \tag{3.26}$$

since $C_2 \approx 0.13$ for the cylindrical trap used in our study. The series on the right hand side describes the inter-particle Coulomb repulsion. We assume that the axial frequency ω_z is tuned into resonance with the detection (LCr) circuit. Thus,

the damping term, proportional to the center-of-mass velocity, is due to energy dissipation in the resistor representing the detection circuit.

For the (transverse) motions in the xy-plane, we have

$$\begin{aligned}\ddot{x}_k \;-\; \omega_c\,\dot{y}_k \;&-\; \frac{1}{2}\,\omega_z^2\,x_k \;-\; 3\,\tilde{C}_4\,\omega_z^2\,(z_k^2-\rho_k^2/4)\,x_k \\ &-\; \frac{15}{2}\,\tilde{C}_6\,\omega_z^2\,(z_k^4-\frac{3}{2}z_k^2\rho_k^2+\frac{1}{8}\rho_k^4)\,x_k \\ &+\; \sqrt{\frac{r_e}{z_o}}\,\omega_M\,\Lambda_M(\mathbf{r}_k)\,\dot{f}_x \;=\; \omega_{ee}^2\sum_{i\neq k}^{N}\frac{(x_k-x_i)}{|\mathbf{r}_{ik}|^3}\,, \qquad (3.27)\end{aligned}$$

where $\mathbf{r}_{ik}=\mathbf{r}_i-\mathbf{r}_k$ and $\rho_k^2=x_k^2+y_k^2$; and

$$\begin{aligned}\ddot{y}_k \;+\; \omega_c\,\dot{x}_k \;&-\; \frac{1}{2}\,\omega_z^2\,y_k \;-\; 3\,\tilde{C}_4\,\omega_z^2\,(z_k^2-\rho_k^2/4)\,y_k \\ &-\; \frac{15}{2}\,\tilde{C}_6\,\omega_z^2\,(z_k^4-\frac{3}{2}z_k^2\rho_k^2+\frac{1}{8}\rho_k^4)\,y_k \\ &+\; \sqrt{\frac{r_e}{z_o}}\,\omega_M\,\Lambda_M(\mathbf{r}_k)\,\dot{f}_y \;=\; \omega_{ee}^2\sum_{i\neq k}^{N}\frac{(y_k-y_i)}{|\mathbf{r}_{ik}|^3}\,. \qquad (3.28)\end{aligned}$$

Coupling terms due to anharmonicity and Coulomb interaction are similar to those for the axial motions. Analogous to interaction with a tuned circuit, the cyclotron oscillations are coupled to a standing wave mode of the cavity. For simplicity, we have assumed the electrons are interacting with an $m=1$ cavity mode near the trap symmetry axis. Then the dimensionless field components (f_x, f_y) are governed by [8,9] :

$$\begin{aligned}\begin{pmatrix}\ddot{f}_x\\ \ddot{f}_y\end{pmatrix} \;+\; \Gamma_M\begin{pmatrix}\dot{f}_x\\ \dot{f}_y\end{pmatrix} \;+\; \omega_M^2\begin{pmatrix}f_x\\ f_y\end{pmatrix} \\ -\;\sqrt{\frac{r_e}{z_o}}\,\omega_M\sum_{k=1}^{N}\Lambda_M(\mathbf{r}_k)\begin{pmatrix}\dot{x}_k\\ \dot{y}_k\end{pmatrix} \;=\; 0, \qquad (3.29)\end{aligned}$$

where $\sqrt{r_e/z_o}\;=\;8.56\times10^{-7}$. The couplings Λ_M are related to those calculated and tabulated for regular geometries of interest [37]. The typical values of frequencies in these equations are provided in Table 3.2.

The standing wave configurations in a cylindrical cavity are described by known analytic functions, allowing us to characterize the electron-cavity coupling

Axial damping width	$\gamma_z/(2\pi)$	(max.) 5 Hz
Collision constant	$\omega_{ee}/(2\pi)$	12×10^3 Hz
Axial frequency	$\omega_z/(2\pi)$	63×10^6 Hz
Cyclotron frequency (swept)	$\omega_c/(2\pi)$	$\sim 100 \times 10^9$ Hz

Table 3.2: Typical values of frequency parameters in the equations of motion.

by the simple functions $\Lambda_M(\mathbf{r}_k)$. For the modes of greatest interest, near the trap symmetry axis, the electron-cavity coupling is given by

$$\Lambda_{1np}(\mathbf{r}_k) \;=\; \Lambda_{1np}\,\sin\left(\frac{p\pi d}{2z_o}z_k + \frac{p\pi}{2}\right). \tag{3.30}$$

The first of two important cases is for an antinode at the midplane, eg. TE_{115}, with

$$\Lambda_{115}(\mathbf{r}_k) \;=\; \Lambda_{115}\,\cos\left(\frac{5\pi d}{2z_o}z_k\right) \quad . \tag{3.31}$$

For a small axial oscillation amplitude, the electron-cavity coupling is a simple constant in this case. The other important case produces cavity mode resonances of a different type (Chapter 4), namely, the case for a node at the midplane, eg. TE_{132}, with

$$\Lambda_{132}(\mathbf{r}_k) \;=\; -\Lambda_{132}\,\sin\left(\frac{\pi d}{z_o}z_k\right) \quad . \tag{3.32}$$

For our apparatus, $d/z_o \;=\; 0.923$. Since these examples are of experimental interest, we provide the values of their parameters in Table 3.3.

The system is parametrically excited by modulating the axial spring constant $m\omega_z^2$, so that the above equations are modified by the substitution

$$\omega_z^2 \longrightarrow \omega_z^2\left[1 + h\cos(\omega_d t)\right]. \tag{3.33}$$

The observed signal is obtained from the voltage induced across the effective detection resistor R

$$V = -\frac{1}{2}\kappa N q\left(\frac{d}{z_o}\right)\dot{Z} \tag{3.34}$$

	TE_{115}	TE_{132}
Λ_M	0.31	0.56
$\Gamma_M/(2\pi)$	144×10^6 Hz	3.8×10^6 Hz
$\omega_M/(2\pi)$	99.513×10^9 Hz	97.525×10^9 Hz

Table 3.3: Parameters for two modes of experimental interest.

which is proportional to the CM oscillation

$$\dot{Z} = \frac{1}{N}\sum_{i=1}^{N} \dot{z}_i. \tag{3.35}$$

A phase-sensitive detector monitors the phase of the coherent response with respect to the pump (Sec. 5.1). For CM energy measurements, this signal is amplified, squared and filtered, giving an output proportional to $\langle \dot{Z}^2 \rangle$.

3.5 Summary

Resonantly cooled by a cavity mode, parametrically-pumped electron oscillators switch abruptly from disordered motions to long-term, coherent CM oscillations as the pump strength exceeds a sharp threshold. Observed collective behavior exhibits Mathieu instability and shares many features characteristic of the nonlinear dynamics in a rigid model. A hyperbolic region of instability in the (h,ω_d) space of the pump is established. Phase degeneracy and hysteresis due to multiplicity of stable states are also observed. Observed maximum CM energy is limited by cavity cooling of internal motions. Nevertheless, dependences of observed parametric resonance lineshapes on anharmonicity are in qualitative agreement with the rigid model.

So far, radiative cooling has been maximized to reveal the collective behaviors of parametrically-pumped electron oscillators. Notwithstanding good agreement with many observed features of the collective motions, the rigid model suffers

from serious over-simplifications. The electron oscillators do not form a rigid structure even at 4K (undriven) because they are "weakly correlated" [67], with the energy in thermal motions being comparable to or exceeding the inter-particle Coulomb energy. Omission of the internal and transverse motions greatly reduces the usefulness of the model in understanding other interesting, non-rigid behaviors. Fortunately, a system of collisionally-coupled, parametrically-pumped electron oscillators is so well-characterized that the full equations of motions can be written down, although not as easily analyzed. We refer to the observed coherent motions in this system as "synchronized motions," to distinguish them from the rigid motions expected of crystal structures. An interesting non-rigid feature, for example, is the extreme sensitivity of the CM energy in synchronized motion to radiative cooling by cavity modes, which opens the way to new experiments involving electron-cavity interaction, as we shall see.